Communication

A Bayesian Compressive Sensing Approach to Robust Near-Field Antenna Characterization

M. Salucci, N. Anselmi, M. D. Migliore, and A. Massa

Abstract—**A novel probabilistic sparsity-promoting method for robust near-field (NF) antenna characterization is proposed. It leverages on the measurements-by-design (MebD) paradigm, and it exploits some *a priori* information on the antenna under test (AUT) to generate an overcomplete representation basis. Accordingly, the problem at hand is reformulated in a compressive sensing (CS) framework as the retrieval of a maximally sparse distribution (with respect to the overcomplete basis) from a reduced set of measured data, and then, it is solved by means of a Bayesian strategy. Representative numerical results are presented to, also comparatively, assess the effectiveness of the proposed approach in reducing the "burden/cost" of the acquisition process and mitigate (possible) truncation errors when dealing with space-constrained probing systems.**

Index Terms—**Antenna measurements, antenna qualification, compressive sensing (CS), near-field (NF) pattern estimation, near-field to far-field (NF-FF) transformation, sparsity retrieval, truncation error.**

I. Introduction

We are nowadays witnessing an extraordinary technological advancement in phased array technology as a key asset to the forthcoming 5G and 6G communications standards [1], [2]. High-performance multi-input/multi-output (MIMO), cognitive, and multibeam architectures will undergo mass production to allow an ubiquitous implementation of the Internet-of-Things (IoT)-based next-generation wireless environments [3]. For a fast and reliable antenna certification at the end of large-scale manufacturing processes [4], [5], over-the-air measurements clearly constitute the most time/cost-effective option. In such a framework, far-field (FF) techniques are one viable and consolidated approach. However, they intrinsically suffer from limitations imposed by outdoor sites, such as the vulnerability to weather conditions and to reflections from (uncontrollable) environmental obstacles/scatterers. Otherwise, near-field (NF) probing methods are alternative solutions that guarantee a higher accuracy and repeatability, thanks to the exploitation of fully controlled indoor environments and the availability of efficient NF-FF transformation strategies [6]–[18], even though they are prone to the so-called "truncation error" caused by the limited extension of the scanning surface (e.g., planar [14], [17], cylindrical [11], spherical [8], and conical [12]) in real anechoic chambers. Moreover, the IEEE recommended practice for NF measurements [19] states that a reliable assessment of the radiation features of an antenna under test (AUT) needs a dense probing step $\Delta\rho$ (i.e., $\Delta\rho \leq (\lambda/2)$, with λ being the free-space wavelength). This results in time-consuming acquisition procedures due to the huge number of scanning positions [7]. An effective recipe to avoid/mitigate such issues is to exploit the available *a priori* information on the AUT. As a matter of fact, several methodologies are based on the representation of the radiation behavior of the AUT in terms of a set of known basis functions defined with accurate full-wave (FW) simulations of the CAD models of the antenna, which are typically available from previous stages of the design process [7], [8]. Accordingly, the NF recovery problem at hand is then reformulated as the retrieval, from a reduced set of measured data, of the expansion coefficients by means of suitable matching strategies [7] or machine learning tools [8]. Within this line of reasoning, the measurements-by-design (MebD) paradigm has been proposed as an effective tool to predict the AUT features by exploiting, unlike abovementioned state-of-the art strategies, the generation of an *overcomplete* basis rather than a minimum-redundancy one [20]–[22]. Thanks to this, it is possible to recast the problem at hand as a sparsity-retrieval one suitable for a fruitful exploitation of the compressive sensing (CS) [20], [23]. As for this latter, it is worth pointing out that a reliable application of standard (deterministic) CS solvers requires a preliminary check of the restricted isometry property (RIP) of the observation operator, which rapidly becomes computationally unaffordable even for small-/medium-scale problems [23]. To overcome this issue, the MebD is mathematically reformulated in this communication within a probabilistic sparsity-promoting framework and then solved by means of a customized Bayesian CS (BCS) strategy that avoids cumbersome assessments of the RIP compliancy [24]. To the best of the authors' knowledge, the main novelties of this research work lie in: 1) the formulation of the NF prediction problem within a highly flexible Bayesian framework dependent on neither the knowledge of the nominal/gold antenna nor on a particular topology of the probing setup and 2) a suitable customization of the BCS to yield a robust and reliable solution of the NF field estimation in a wide range of applicative scenarios.

The outline of this communication is given as follows. The mathematical formulation of the NF antenna characterization problem

Manuscript received 14 July 2021; revised 12 April 2022; accepted 30 April 2022. Date of publication 30 May 2022; date of current version 6 October 2022. This work has been partially supported by the Italian Ministry of Education, University, and Research within the Program PRIN 2017 (CUP: E64I19002530001) for the Project EMvisioning (Grant no. 2017HZJXSZ), within the Program "Smart cities and communities and Social Innovation" (CUP: E44G14000040008) for the Project "SMARTOUR" (Grant no. SCN_00166), within the Program PON R&I 2014-2020 for the Project "MIT-IGO" (Grant no. ARS01_00964), and under Grant "Dipartimenti di Eccellenza (2018-2022)". Moreover, it benefited from the networking activities carried out within the Project SPEED (Grant No. 61721001) funded by National Science Foundation of China under the Chang-Jiang Visiting Professorship Program. *(Corresponding author: A. Massa.)*

M. Salucci and N. Anselmi are with the ELEDIA Research Center (ELEDIA@UniTN), DICAM—Department of Civil, Environmental, and Mechanical Engineering, University of Trento, 38123 Trento, Italy (e-mail: marco.salucci@unitn.it; nicola.anselmi.1@unitn.it).

M. D. Migliore is with the ELEDIA Research Center (ELEDIA@UniCAS—DIEI), University of Cassino and Southern Lazio, I-03043 Cassino, Italy (e-mail: donald.migliore@eledia.org).

A. Massa is with the ELEDIA Research Center (ELEDIA@UniTN), DICAM—Department of Civil, Environmental, and Mechanical Engineering, University of Trento, 38123 Trento, Italy, also with the ELEDIA Research Center (ELEDIA@UESTC), School of Electronic Engineering, University of Electronic Science and Technology of China, Chengdu 611731, China, and also with the ELEDIA Research Center (ELEDIA@TSINGHUA), Tsinghua University, Beijing 100084, China (e-mail: andrea.massa@unitn.it).

Color versions of one or more figures in this communication are available at https://doi.org/10.1109/TAP.2022.3177528.

Digital Object Identifier 10.1109/TAP.2022.3177528

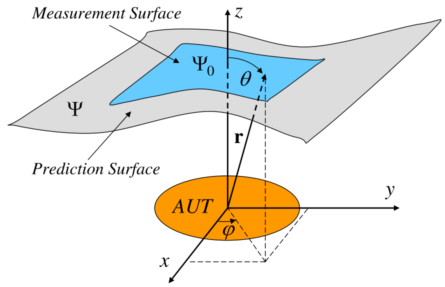

Fig. 1. Pictorial sketch of the NF antenna characterization scenario.

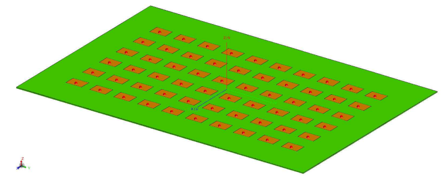

Fig. 2. *Numerical validation* ($N = 60$)—3-D view of the FEKO FW model of the array composed by $N = (N_x \times N_y) = (6 \times 10)$ rectangular probe-fed microstrip patches working at $f = 3.6$ [GHz] ($(l_x, l_y) = (2.2 \times 10^{-1}, 3.3 \times 10^{-1})$ [λ], $\varepsilon_r = 4.7$, $\tan\delta = 1.4 \times 10^{-2}$, and $h = 1.9 \times 10^{-2}$ [λ]).

and its BCS-based solution method is detailed in Section II. Representative results are shown and discussed in Section III to assess the effectiveness and the potentialities of the proposed approach. Finally, some conclusions are drawn in Section IV.

II. Mathematical Formulation

To faithfully retrieve the FF pattern features of an AUT by means of NF-FF transformation rules [18], the radiated tangential electric field distribution must be accurately estimated over a sufficiently large surface Ψ (see Fig. 1) to limit as much as possible the so-called "truncation error" [16]. Generally speaking, Ψ is sampled according to Nyquist's rule by choosing $\Delta\rho = (\lambda/2)$ ($\Delta\rho$ being the sampling rate along a generic direction of the surface Ψ) [19] for yielding the set of T locations $\mathcal{T} = \{\mathbf{r}_t \in \Psi;\ t = 1, \ldots, T\}$. Let us express the NF distribution in $\mathcal{T}$, $\underline{\widetilde{E}} = \{\widetilde{E}(\mathbf{r}_t);\ t = 1, \ldots, T\}$, as the linear combination of B properly built basis vectors, $\underline{\underline{\mathcal{A}}} = \{\underline{\mathcal{A}}_b;\ b = 1, \ldots, B\}$ [$\underline{\mathcal{A}}_b = \{\mathcal{A}_b(\mathbf{r}_t);\ t = 1, \ldots, T\}$ being the bth ($b = 1, \ldots, B$) one] through a set of unknown coefficients $\underline{w} = \{w_b \in \mathbb{C};\ b = 1, \ldots, B\}$

$$\underline{\widetilde{E}} = \underline{\underline{\mathcal{A}}}\, \underline{w}. \tag{1}$$

According to the MebD paradigm [20], the basis $\mathcal{A}$ is defined by exploiting the *a priori* information on the AUT through the following procedure.

1) *Uncertainty Identification:* Identify the set of C uncertainty factors that can cause a deviation of the AUT radiation features from the ideal/gold ones (e.g., defects of the beamforming network and manufacturing tolerances). For each cth ($c = 1, \ldots, C$) uncertainty descriptor, χ_c defines a suitable (physically admissible) variation range $[\chi_c^{\min}, \chi_c^{\max}]$. Finally, let $c = 1$ and $b = 0$, and go to *Step 2*.
2) *Overcomplete Basis Generation:* Loop ($c = 1, \ldots, C$).
   a) Uniformly sample the cth descriptor to form the set of K_c configurations $\underline{\chi}_c = \{\chi_c^{(k)};\ k = 1, \ldots, K_c\}$, with the kth one being
   $$\chi_c^{(k)} = \chi_c^{\min} + (k-1)\frac{\left(\chi_c^{\max} - \chi_c^{\min}\right)}{(K_c - 1)}. \tag{2}$$
   b) Run K_c FW simulations of the AUT to fill the set of NF distributions $\underline{\underline{\mathcal{E}}}_c = \{\underline{\mathcal{E}}_c^{(k)};\ k = 1, \ldots, K_c\}$, $\underline{\mathcal{E}}_c^{(k)} = \{E(\mathbf{r}_t|\chi_c^{(k)});\ t = 1, \ldots, T\}$ being the sampled NF distribution in Ψ for an AUT whose cth uncertainty descriptor has a value equal to the kth sample of its variation range (i.e., $\chi_c = \chi_c^{(k)}$).
   c) Apply the truncated singular value decomposition (TSVD) to $\underline{\underline{\mathcal{E}}}_c$
   $$\underline{\underline{\mathcal{E}}}_c = \underline{\underline{\mathcal{U}}}_c \underline{\underline{\Sigma}}_c \left(\underline{\underline{\mathcal{V}}}_c\right)^* \tag{3}$$
   where $\underline{\underline{\mathcal{U}}}_c = \{\underline{\mathcal{U}}_c^{(q)};\ q = 1, \ldots, Q_c\}$ and $\underline{\underline{\mathcal{V}}}_c = \{\underline{\mathcal{V}}_c^{(q)};\ q = 1, \ldots, Q_c\}$ are the first left and right singular vectors associated with the Q_c singular values, $\underline{\sigma}_c = \{\sigma_c^{(q)};\ q = 1, \ldots, Q_c\}$, above the noise threshold, respectively, while $\underline{\underline{\Sigma}}_c = \mathrm{diag}\{\underline{\sigma}_c\}$ and $(\,.\,)^*$ stands for the complex conjugate.
   d) Add the Q_c left singular vectors to the basis $\underline{\underline{\mathcal{A}}}$ by letting
   $$\underline{\mathcal{A}}_{(b+q)} \leftarrow \underline{\mathcal{U}}_c^{(q)}; \quad q = 1, \ldots, Q_c \tag{4}$$
   and then update the index b [$b \leftarrow (b + Q_c)$].
   e) If $c = C$, then terminate the iterative loop and output the set of B ($B = \sum_{c=1}^{C} Q_c$) bases, $\underline{\underline{\mathcal{A}}}$. Otherwise, let $c \leftarrow (c+1)$, and go to Step 2(a).

As for the unknown coefficient vector $\underline{w}$ in (1), it is retrieved from a limited set of NF data collected over the measurement surface $\Psi_0 \subseteq \Psi$ (see Fig. 1). Toward this end, let us assume that the field radiated by the AUT is measured over a subset of $M \ll T$ probing locations $\mathcal{M} = \{\mathbf{r}_m \in \Psi_0;\ m = 1, \ldots, M\}$ ($\mathcal{M} \subset \mathcal{T}$) to collect the data vector $\underline{d} = \{E(\mathbf{r}_m);\ m = 1, \ldots, M\}$. Accordingly, $\underline{w}$ can be computed by solving the following system of equations:

$$\underline{\underline{\mathcal{A}}}'\, \underline{w} - \underline{d} = \underline{g} \tag{5}$$

where the observation operator $\underline{\underline{\mathcal{A}}}' = \{\underline{\mathcal{A}}'_b;\ b = 1, \ldots, B\}$ is derived from $\underline{\underline{\mathcal{A}}}$ by setting each bth ($b = 1, \ldots, B$) column to $\underline{\mathcal{A}}'_b = \{\mathcal{A}'_b(\mathbf{r}_m);\ m = 1, \ldots, M\} = \Gamma\{\underline{\mathcal{A}}_b\}$, $\Gamma\{\,.\,\}$ being an operator extracting the M entries of $\underline{\mathcal{A}}_b$ associated with the probing positions of $\mathcal{M}$. Moreover, the vector $\underline{g} = \{g(\mathbf{r}_m);\ m = 1, \ldots, M\}$ in (5) models the presence of an additive noise blurring the data.

It is worth pointing out that, in real scenarios, only a very limited subset (or none) of the C uncertainties affects the measured AUT. Therefore, the solution vector $\underline{w}$ is generally intrinsically sparse (i.e., $\|\underline{w}\|_0 \ll B$, $\|\,.\,\|_0$ being the ℓ_0-norm), and effective solutions of (5) can be obtained within the CS framework by exploiting a probabilistic Bayesian approach [24] to avoid the RIP check. More in detail, the linear system of equations (5) is first rearranged in the following form:

$$\underline{\underline{A}}\,\underline{\omega} - \underline{\delta} = \underline{\gamma} \tag{6}$$

where

$$\underline{\underline{A}} = \begin{bmatrix} \Re\left\{\underline{\underline{\mathcal{A}}}'\right\} & -\Im\left\{\underline{\underline{\mathcal{A}}}'\right\} \\ \Im\left\{\underline{\underline{\mathcal{A}}}'\right\} & \Re\left\{\underline{\underline{\mathcal{A}}}'\right\} \end{bmatrix} \tag{7}$$

$\Re\{\,.\,\}$ and $\Im\{\,.\,\}$ being the real and imaginary part, respectively, while $\underline{\omega} \triangleq [\Re\{\underline{w}\}, \Im\{\underline{w}\}]$, $\underline{\delta} \triangleq [\Re\{\underline{d}\}, \Im\{\underline{d}\}]$, and $\underline{\gamma} \triangleq [\Re\{\underline{g}\}, \Im\{\underline{g}\}]$ are column vectors. Accordingly, the sparsest guess of $\underline{\omega}$ ($\underline{\widetilde{\omega}} \triangleq \{\widetilde{\omega}_b;\ b = 1, \ldots, (2 \times B)\}$) that maximizes the *a posteriori* probability

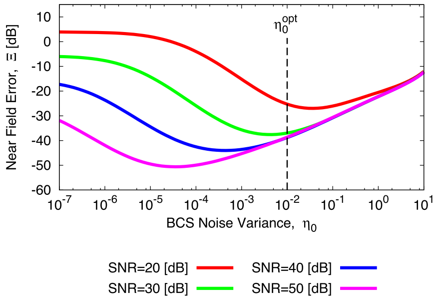

Fig. 3. *BCS calibration* ($H = 7$ [λ], $L_\Psi = L_{\Psi_0} = 20$ [λ], $M = 25$, $T = 1681$, $N = 60$, $|\zeta_3| = 0.45$, $\angle\zeta_3 = (\pi/3)$ [rad], and $SNR \in [20, 50]$ [dB])—behavior of the NF integral error, Ξ, as a function of the BCS parameter η_0.

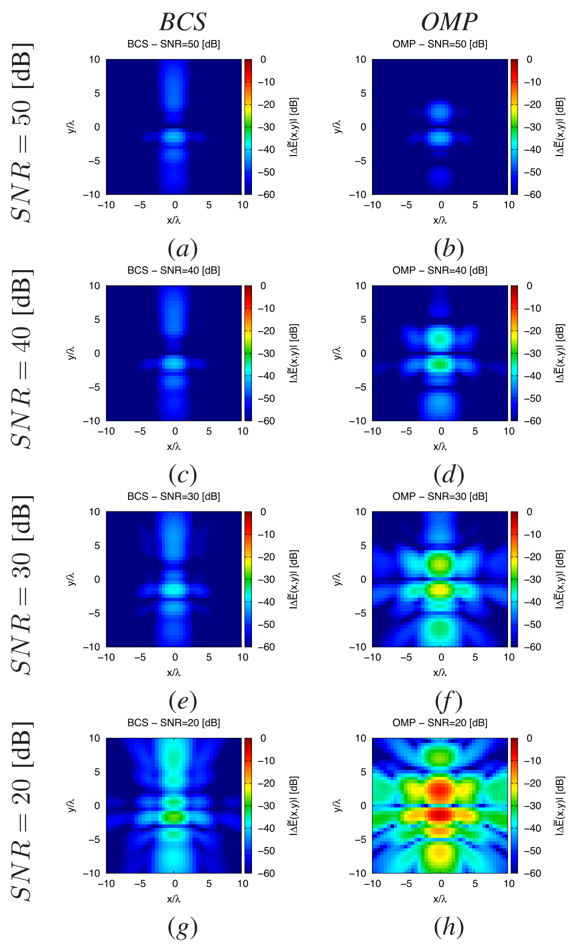

Fig. 4. *Numerical validation* ($H = 7$ [λ], $L_\Psi = L_{\Psi_0} = 20$ [λ], $M = 25$, $T = 1681$, $N = 60$, $|\zeta_3| = 0.45$, and $\angle\zeta_3 = (\pi/3)$ [rad])—NF error maps $|\Delta\widetilde{E}(\mathbf{r})|$ yielded by (a), (c), (e), and (g) BCS and (b), (d), (f), and (h) OMP when processing noisy data with (a) and (b) $SNR = 50$ [dB], (c) and (d) $SNR = 40$ [dB], (e) and (f) $SNR = 30$ [dB], and (g) and (h) $SNR = 20$ [dB].

$\mathcal{P}(\underline{\omega}|\underline{\delta})$ is computed as follows [24]:

$$\underline{\widetilde{\omega}} = \frac{1}{\widetilde{\eta}}\left[\frac{\left(\underline{\underline{A}}\right)^*\underline{\underline{A}}}{\widetilde{\eta}} + \text{diag}\left\{\underline{\widetilde{\tau}}\right\}\right]^{-1}\left(\underline{\underline{A}}\right)^*\underline{\delta}. \quad (8)$$

In (8), $\widetilde{\eta}$ and $\underline{\widetilde{\tau}}$ ($\underline{\widetilde{\tau}} = \{\widetilde{\tau}_b;\ b = 1, \ldots, (2\times B)\}$) are the estimated BCS noise variance and the BCS hyperparameters, respectively. They are determined with a fast relevant vector machine (RVM)-based local search strategy [23] by maximizing the following likelihood function:

$$\Phi\left(\eta,\ \underline{\tau}\right) = \left\{-\frac{1}{2}\left[2M\log 2\pi + \log\left|\underline{\underline{\Omega}}\right| + \left(\underline{\delta}\right)^*\left(\underline{\underline{\Omega}}\right)^{-1}\underline{\delta}\right]\right\} \quad (9)$$

starting from initial guess of the BCS noise variance, η_0. In (9), $|\,.\,|$ is the matrix determinant, $\underline{\underline{\Omega}} = \eta\underline{\underline{I}} + \underline{\underline{A}}(\text{diag}\{\underline{\tau}\})^{-1}(\underline{\underline{A}})^*$, M is the number of probing locations, and $\underline{\underline{I}}$ is the identity matrix. Finally, the solution of (5) is computed by rearranging the entries of the BCS vector (8) into the complex-valued expansion weights as follows:

$$\underline{\widetilde{w}} = \left\{\left(\widetilde{\omega}_b + j\widetilde{\omega}_{b+B}\right);\ b = 1, \ldots, B\right\} \quad (10)$$

$j = (-1)^{1/2}$ being the imaginary unit, while the corresponding estimated field radiated by the AUT at the prediction locations $\mathcal{T}$ is retrieved by inputting (10) into (1).

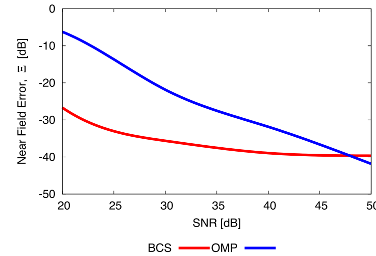

Fig. 5. *Numerical validation* ($H = 7$ [λ], $L_\Psi = L_{\Psi_0} = 20$ [λ], $M = 25$, $T = 1681$, $N = 60$, $|\zeta_3| = 0.45$, $\angle\zeta_3 = (\pi/3)$ [rad], and $SNR \in [20, 50]$ [dB])—behavior of the NF integral error, Ξ, as a function of the SNR.

III. Numerical Validation

The objective of this section is twofold. On the one hand, representative results from an exhaustive numerical study are reported to assess the effectiveness of the proposed BCS-based approach also in comparison with a previously published state-of-the-art CS approach based on the orthogonal matching pursuit (OMP) [20]. On the other hand, this section is aimed at providing the interested readers/users with some useful guidelines for its optimal application.

As for the results, besides a pictorial representation of the NF field reconstructions, the NF integral error

$$\Xi \triangleq \frac{\sum_{t=1}^{T}\left|E\left(\mathbf{r}_t\right) - \widetilde{E}\left(\mathbf{r}_t\right)\right|^2}{\sum_{t=1}^{T}\left|E\left(\mathbf{r}_t\right)\right|^2} \quad (11)$$

is computed to provide a quantitative index of the "solution quality."

In the benchmark scenario, the reference AUT is a linearly polarized [i.e., $E(\mathbf{r}) = E_x(\mathbf{r})\widehat{\mathbf{x}}$] planar phased array arranged on the $(x,\ y)$ plane, and it is composed by $N = (N_x \times N_y) = (6 \times 10) = 60$ rectangular probe-fed microstrip patches working at $f = 3.6$ [GHz]. The radiators have dimensions $(l_x,\ l_y) = (2.2 \times 10^{-1},\ 3.3 \times 10^{-1})$ [λ] and they are etched in a $(\lambda/2)$-spaced square lattice on a dielectric substrate with relative permittivity $\varepsilon_r = 4.7$, loss tangent $\tan\delta = 1.4 \times 10^{-2}$, and thickness $h = 1.9 \times 10^{-2}$ [λ]. Moreover, the feeding architecture consists of $S = N_y = 10$ uniformly excited clusters/planks corresponding to the rows of the array, the nominal/gold excitations being set to $\zeta_s = 1.0$ ($s = 1, \ldots, S$). As for the NF setup, Ψ_0 is a square plane of side $L_{\Psi_0} = 20$ [λ] placed $H = 7$ [λ] above the AUT top surface. As for the probing location set $\mathcal{M}$, it consists of $M = (M_x \times M_y) = (5 \times 5) = 25$ positions uniformly distributed over Ψ_0 with a step of $\Delta_x^{\mathcal{M}} = \Delta_y^{\mathcal{M}} = 5$ [λ] [20]. To account for mutual coupling effects, the basis $\underline{\underline{A}}$ has been built by modeling the AUT within the Altair FEKO FW simulation environment [25] by considering a $(\lambda/2)$-sampled

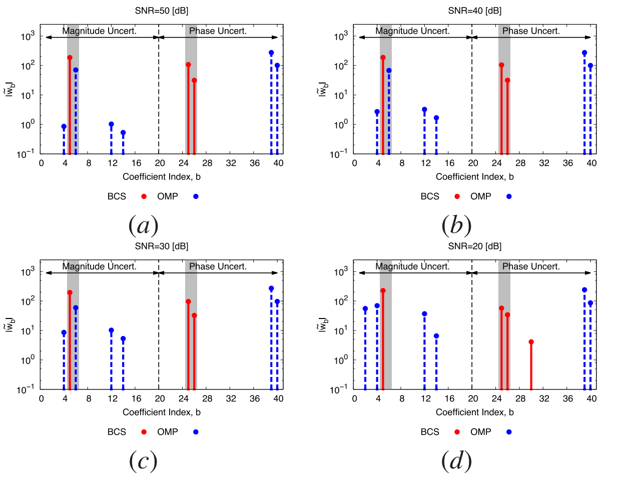

Fig. 6. *Numerical validation* ($H = 7$ [λ], $L_\Psi = L_{\Psi_0} = 20$ [λ], $M = 25$, $T = 1681$, $N = 60$, $|\zeta_3| = 0.45$, and $\angle\zeta_3 = (\pi/3)$ [rad])—magnitude of the retrieved expansion coefficients, $|\widetilde{\omega}_b|$, $b = 1, \ldots, B$, outputted by the BCS and the OMP methods when processing noisy data with (a) SNR = 50 [dB], (b) SNR = 40 [dB], (c) SNR = 30 [dB], and (d) SNR = 20 [dB].

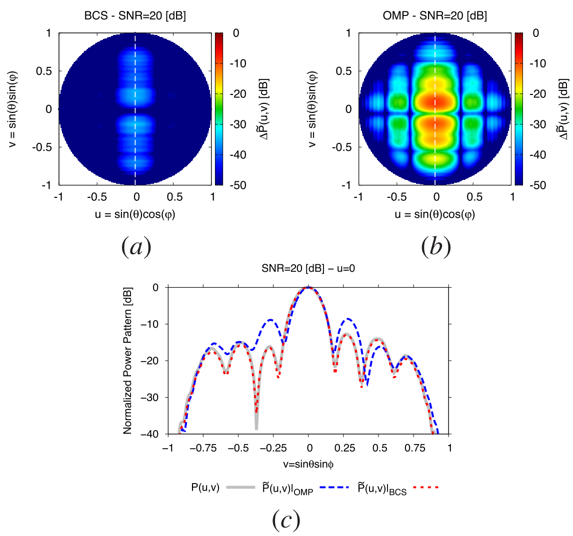

Fig. 7. *Numerical validation* ($H = 7$ [λ], $L_\Psi = L_{\Psi_0} = 20$ [λ], $M = 25$, $T = 1681$, $N = 60$, $|\zeta_3| = 0.45$, $\angle\zeta_3 = (\pi/3)$ [rad], and $SNR = 20$ [dB])—FF error maps, $|\Delta\widetilde{P}(u, v)|$, yielded by (a) BCS and (b) OMP methods. Estimated power patterns along the ($u = 0$)-cut (c).

(i.e., $\Delta x = \Delta y = \Delta\rho$) prediction surface $\Psi = \Psi_0$ [$T = (T_x \times T_y) = (41 \times 41) = 1681 \Rightarrow (M/T) \approx 1.5\%$]. The average time for an FW simulation of the array model, whose 3-D CAD layout is shown in Fig. 2, is equal to $\Delta t_{FW} \approx 3$ [min] on a PC equipped with an Intel Xeon CPU @ 3.5 [GHz] and 64 [GB] of RAM memory. For the numerical study, the antenna at hand is assumed to be potentially affected by $C = (2 \times S) = 20$ deviations from the gold one, which are associated with nonidealities on both the magnitude ($\chi_c = |\zeta_c|$, $[\chi_c^{\min}, \chi_c^{\max}] = [0, 1]$, and $c = 1, \ldots, S$) and the phase ($\chi_c = \angle\zeta_c$, $[\chi_c^{\min}, \chi_c^{\max}] = [-\pi, \pi]$, and $c = S+1, \ldots, C$) of the excitations of each sth ($s = 1, \ldots, S$) subarray. According to the MebD guidelines [20], $K_c = 7$ simulations have been performed for each cth ($c = 1, \ldots, C$) uncertainty factor to yield a basis of $B = 40$ vectors, $Q_c = 2$ being the number of truncated singular values for each cth index. Accordingly, a total FW simulation time of $\Delta t \approx 420$ [min] has been required to build the overcomplete basis.

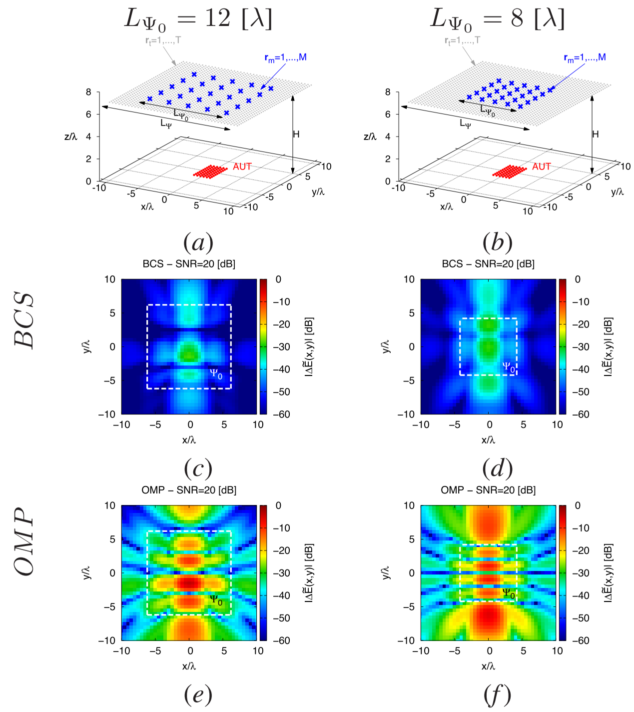

Fig. 8. *Numerical validation* ($H = 7$ [λ], $L_\Psi = 20$ [λ], $M = 25$, $T = 1681$, $N = 60$, $|\zeta_3| = 0.45$, $\angle\zeta_3 = (\pi/3)$ [rad], and $SNR = 20$ [dB])—(a) and (b) measurement setup and (c)–(f) NF error maps yielded by (c) and (d) BCS and (e) and (f) OMP methods when considering a truncated NF probing region of side (a), (c), and (e) $L_{\Psi_0} = 12$ [λ] and (b), (d), and (f) $L_{\Psi_0} = 8$ [λ].

A preliminary calibration of the BCS setup has been carried out by assuming as reference an AUT affected by a partial failure on the excitation coefficient of the $s = 3$rd row (i.e., $|\zeta_3| = 0.45$ and $\angle\zeta_3 = (\pi/3)$ [rad]). Toward this end, the initial guess of the BCS noise variance, η_0, for the RVM-based maximization of (9) has been varied within the range $10^{-7} \leq \eta_0 \leq 10$, and the value of the NF integral error (11) has been computed for different noise levels ($SNR \in [20, 50]$ [dB]). The outcomes of this analysis are summarized in Fig. 3. As expected, the optimal value of η_0 depends on the SNR (e.g., $\eta_0^{opt}|_{SNR=50\,[\mathrm{dB}]} < \eta_0^{opt}|_{SNR=40\,[\mathrm{dB}]} < \eta_0^{opt}|_{SNR=30\,[\mathrm{dB}]} < \eta_0^{opt}|_{SNR=20\,[\mathrm{dB}]}$, being $\eta_0^{opt}|_{SNR} = \arg[\min_{\eta_0}(\Xi(\eta_0)|_{SNR})]$) since, by definition, the larger is the noise variance, the lower is the SNR. On the other hand, no *a priori* accurate information on the noise level is available in several practical cases; thus, an optimal tradeoff value has been chosen as $\eta_0^{opt} \triangleq (\int \eta_0^{opt}|_{SNR} dSNR / \int dSNR)$ and it has been set here to $\eta_0^{opt} = 10^{-2}$ (see Fig. 3). To assess the reliability of such a calibration in general operative conditions, the normalized error map (i.e., $|\Delta\widetilde{E}(\mathbf{r}_t)| \triangleq |\widetilde{E}(\mathbf{r}_t) - E(\mathbf{r}_t)| / \max_{\mathbf{r}_t} |E(\mathbf{r}_t)|$, $\mathbf{r}_t \in \mathcal{T}$, $t = 1, \ldots, T$) is reported in Fig. 4 (left column) for different SNRs. It turns out that the NF estimation error is always very small and upper bounded to $\max_{\mathbf{r}_t \in \mathcal{T}} |\Delta\widetilde{E}(\mathbf{r}_t)||_{SNR=20\,[\mathrm{dB}]} = -27.2$ [dB] [see Fig. 4(g)]. For comparisons, the maps yielded with the OMP-based implementation [20] are reported (see Fig. 4—right column), as well, to pictorially underline the better performance of the BCS approach that is quantitatively confirmed by the plots of the corresponding errors (see Fig. 5). As a matter of fact, the BCS is more robust to the noise, and it remarkably reduces the NF error especially in the worst case conditions [e.g., $SNR = 20$ [dB] - $(\Xi|_{SNR=20\,[\mathrm{dB}]}^{BCS} / \Xi|_{SNR=20\,[\mathrm{dB}]}^{OMP}) \approx -21$ [dB], and Fig. 4(g) versus Fig. 4(h)]. Independently on the SNR, the BCS provides more sparse

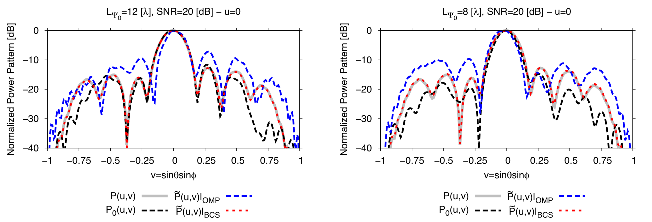

(a) (b)

Fig. 9. *Numerical validation* ($H = 7$ [λ], $L_\Psi = 20$ [λ], $M = 25$, $T = 1681$, $N = 60$, $|\zeta_3| = 0.45$, $\angle\zeta_3 = (\pi/3)$ [rad], and $SNR = 20$ [dB])—actual, $P(u, v)$, truncated, $P_0(u, v)$, and estimated, $\widetilde{P}(u, v)$, power patterns along the ($u = 0$)-cut when (a) $L_{\Psi_0} = 12$ [λ] and (b) $L_{\Psi_0} = 8$ [λ].

solutions than the OMP (i.e., $\|\underline{\widetilde{w}}^{BCS}\|_0 < \|\underline{\widetilde{w}}^{OMP}\|_0$) and, unlike this latter, the retrieved nonnull entries of $\underline{\widetilde{w}}^{BCS}$ when $SNR >$ 20 [dB] are in correspondence with the four redundant[1] basis vectors associated with the uncertainty factors affecting the actual AUT and highlighted with the vertical gray bar in Fig. 6. As a matter of fact, $|\widetilde{w}_b^{BCS}| > 0$ when $b = 5$ (i.e., the first column of $\underline{\underline{A}}$ linked to a variation of $|\zeta_3|$), $b = 25$, and $b = 26$ (i.e., the basis vectors corresponding to $\angle\zeta_3$), as shown in Fig. 6(a)–(c). This points out that the BCS does not only improve the estimation accuracy of the NF distribution in $\mathcal{T}$ of the OMP, but it also generally provides the information on which defect/anomaly is deviating the AUT pattern from the ideal one.

To investigate the impact of the NF prediction on the FF characterization of the AUT, let us analyze the error maps of the mismatch between the actual, $P(u, v) = \mathcal{F}\{E(\mathbf{r})\}$, and the retrieved, $\widetilde{P}(u, v) = \{\widetilde{E}(\mathbf{r})\}$, power patterns, $|\Delta\widetilde{P}(u, v)| \triangleq |P(u, v) - \widetilde{P}(u, v)|$, $u = \sin\theta\cos\phi$ and $v = \sin\theta\sin\phi$ being the direction cosines [$(u^2 + v^2) \leq 1$], while $\mathcal{F}\{.\}$ stands for the NF-FF operator. As a representative example, Fig. 7(a) and (b) refers to the case with $SNR = 20$ [dB]. As expected, the error of the BCS is smaller than that the OMP as a direct consequence of the more accurate NF reconstruction [see Fig. 4(g) versus Fig. 4(h) $\Rightarrow$ Fig. 7(a) versus Fig. 7(b)]. Quantitatively, the maximum FF deviation $|\Delta\widetilde{P}(u, v)|_{\max}$ ($|\Delta\widetilde{P}(u, v)|_{\max} \triangleq \max_{(u^2+v^2)\leq 1} |\Delta\widetilde{P}(u, v)|$) is equal to $|\Delta\widetilde{P}(u, v)|_{\max}^{BCS} = -34.2$ [dB] [see Fig. 7(a)] and $|\Delta\widetilde{P}(u, v)|_{\max}^{OMP} = -8.8$ [dB] [see Fig. 7(b)], respectively. Such outcomes are further confirmed by the comparison between the actual and retrieved power patterns along the most critical cut (i.e., $u = 0$) in Fig. 7(c). Indeed, the OMP curve clearly shows larger and nonnegligible distortions of the pattern outside the main lobe region. As for the time required to collect the data, a standard procedure would require $M^{STD} = 1681$ samples on a uniform lattice with $M_y^{STD} = 41$ rows and $M_x^{STD} = 41$ columns. If the same time is needed to scan a vertical line either with $M_y^{STD} = 41$ or $M_y = 5$ measurements, the scanning time would be reduced by $(41/5) = 8.2$ times. However, it would be also possible to exploit a fixed NF system with $M = 25$ probes, performing "single-shot" measurements in fractions of seconds.

Finally, let us investigate on the effectiveness of the proposed method in mitigating the "truncation error." Toward this end, the side of the measurement plane Ψ_0 has been shrinked to $L_{\Psi_0} = 12$ [λ] [see Fig. 8(a)]. Regardless of the reduction of the probing area [i.e., the area has been reduced by a factor of $(\Psi_0/\Psi) = 0.36$] and the measurement points [i.e., the saving in number of probing positions is 98.5% with respect to a standard ($\lambda/2$) sampling] and the noise level ($SNR = 20$ [dB]), the BCS is very accurate in estimating the NF field distribution [see Fig. 8(c)], and it clearly overcomes the OMP [see Fig. 8(c) versus Fig. 8(e)] as pointed out by the corresponding values of the integral error (i.e., $\Xi|_{\Psi_0=12\,[\lambda]}^{BCS} = -25.1$ [dB] versus $\Xi|_{\Psi_0=12\,[\lambda]}^{OMP} = -4.5$ [dB]). Similar conclusions can be drawn also in the very challenging case of $L_{\Psi_0} = 8$ [λ] [i.e., the measurement area is reduced by a factor of $(\Psi_0/\Psi) = 0.16$] with errors equal to $\Xi|_{\Psi_0=8\,[\lambda]}^{BCS} = -22.8$ [dB] [see Fig. 8(d)] and $\Xi|_{\Psi_0=8\,[\lambda]}^{OMP} = -2.7$ [dB]. For completeness, the ($u = 0$)-cut of the corresponding FF patterns is shown in Fig. 9, where the transformed pattern from the actual truncated NF data, $P_0(u, v) = \mathcal{F}\{E(\mathbf{r})|_{\mathbf{r}\in\Psi_0}\}$, is reported as well, to better highlight the reconstruction capabilities of the BCS solution technique and its superior capability of mitigating the truncation error.

[1]Since the basis set is overcomplete, an NF field prediction needs at least one component for each uncertainty factor. In this example, there are two nonnull entries for each of the $C = 2$ uncertainty factors. Therefore, one entry for each factor is mandatory.

IV. Conclusion

A novel antenna characterization technique, which leverages on the MebD paradigm and a suitable implementation of the BCS, has been proposed to faithfully recover the NF field distribution generated by an AUT starting from a limited set of measurements. More specifically, the NF reconstruction problem has been reformulated within a probabilistic sparsity-promoting framework to bypass the cumbersome check of the RIP compliancy of the measurement operator. An analysis of the dependence of the BCS performance on its calibration setup has been carried out to derive some practical guidelines for its reliable application. The potentialities and limitations of the proposed method have been assessed in a comparative numerical validation under different operative conditions. The main outcomes from the numerical analyses are given as follows.

1) The proposed BCS-based method faithfully retrieves the NF behavior of the AUT with a remarkable robustness to the noise. This implies a reliable characterization of the FF radiation pattern of the AUT in the whole visible range.
2) Unlike other state-of-the-art CS alternative methods, it not only yields an accurate NF/FF prediction of the radiated field but it also provides information on which uncertainties are causing the deviations of the AUT pattern from the gold one.
3) It exhibits excellent performance in mitigating the truncation error caused by the limited-extension probing area.

Finally, it is worth pointing out that the proposed method is general, and it is extendable to any type of antenna or field distribution. Moreover, it can be applied to any scanning surface, being not limited to the standard ones (i.e., planar, cylindrical [22], or spherical) for antenna characterization, provided that the most part of the energy radiated by the AUT is collected when generating the overcomplete basis. The method is also robust with respect to probe positioning errors and truncated data due to a limited scanning area [21]. Indeed, the set of atoms in the overcomplete dictionary (i.e., the basis vectors forming the columns of $\underline{\underline{A}}$) is a discrete set that can only represent a specific subset of possible patterns according to the *a priori* information about the problem. As long as the uncertainty factors (noise, truncation errors, sampling positioning errors, and so on) do not bring the measured field configuration closer to a possible wrong *a priori* configuration, the reconstruction is not affected by them. An experimental assessment of the proposed method will be the object of future works.

Acknowledgment

A. Massa wishes to thank E. Vico for her never-ending inspiration, support, guidance, and help.

REFERENCES

[1] J. S. Herd and M. D. Conway, "The evolution to modern phased array architectures," *Proc. IEEE*, vol. 104, no. 3, pp. 519–529, Mar. 2016.

[2] P. Rocca, G. Oliveri, R. J. Mailloux, and A. Massa, "Unconventional phased array architectures and design methodologies—A review," *Proc. IEEE*, vol. 104, no. 3, pp. 544–560, Mar. 2016.

[3] F. Guo, F. R. Yu, H. Zhang, X. Li, H. Ji, and V. C. M. Leung, "Enabling massive IoT toward 6G: A comprehensive survey," *IEEE Internet Things J.*, vol. 8, no. 15, pp. 11891–11915, Aug. 2021.

[4] Y. Qi *et al.*, "5G over-the-air measurement challenges: Overview," *IEEE Trans. Electromagn. Compat.*, vol. 59, no. 6, pp. 1661–1670, Dec. 2017.

[5] K. Remley *et al.*, "Measurement challenges for 5G and beyond: An update from the national institute of standards and technology," *IEEE Microw. Mag.*, vol. 18, no. 5, pp. 41–56, Jul. 2017.

[6] J. Lundgren, J. Helander, M. Gustafsson, D. Sjoberg, B. Xu, and D. Colombi, "A near-field measurement and calibration technique: Radio-frequency electromagnetic field exposure assessment of millimeter-wave 5G devices," *IEEE Antennas Propag. Mag.*, vol. 63, no. 3, pp. 77–88, Jun. 2021.

[7] G. Giordanengo, M. Righero, F. Vipiana, G. Vecchi, and M. Sabbadini, "Fast antenna testing with reduced near field sampling," *IEEE Trans. Antennas Propag.*, vol. 62, no. 5, pp. 2501–2513, May 2014.

[8] R. R. Alavi and R. Mirzavand, "Range extension in partial spherical near-field measurement using machine learning algorithm," *IEEE Antennas Wireless Propag. Lett.*, vol. 19, no. 11, pp. 2003–2007, Nov. 2020.

[9] D. Slater, *Near Field Antenna Measurements*. New York, NY, USA: Artech House, 1991.

[10] F. Las-Heras, M. R. Pino, S. Loredo, Y. Alvarez, and T. K. Sarkar, "Evaluating near-field radiation patterns of commercial antennas," *IEEE Trans. Antennas Propag.*, vol. 54, no. 8, pp. 2198–2207, Aug. 2006.

[11] F. Ferrara, C. Gennarelli, R. Guerriero, G. Riccio, and C. Savarese, "Extrapolation of the outside near-field data in the cylindrical scanning," *Electromagnetics*, vol. 28, no. 5, pp. 333–345, 2008.

[12] D. Leatherwood, "Conical near-field antenna measurement system," *IEEE Antennas Propag. Mag.*, vol. 50, no. 6, pp. 212–218, Dec. 2008.

[13] R. G. Yaccarino, L. I. Williams, and Y. Rahmat-Samii, "Linear spiral sampling for the bipolar planar near-field antenna measurement technique," *IEEE Trans. Antennas Propag.*, vol. 44, no. 7, pp. 1049–1051, Jul. 1996.

[14] X. Li, T. Zhang, M. Wei, and L. Yang, "Reduction of truncation errors in planar near-field antenna measurements using improved Gerchberg–Papoulis algorithm," *IEEE Trans. Instrum. Meas.*, vol. 69, no. 9, pp. 5972–5974, Sep. 2020.

[15] O. M. Bucci, G. D'Elia, and M. D. Migliore, "A new strategy to reduce the truncation error in near-field/far-field transformations," *Radio Sci.*, vol. 35, no. 1, pp. 3–17, Jan. 2000.

[16] O. M. Bucci and M. D. Migliore, "A new method for avoiding the truncation error in near-field antennas measurements," *IEEE Trans. Antennas Propag.*, vol. 54, no. 10, pp. 2940–2952, Oct. 2006.

[17] E. Martini, O. Breinbjerg, and S. Maci, "Reduction of truncation errors in planar near-field aperture antenna measurements using the Gerchberg–Papoulis algorithm," *IEEE Trans. Antennas Propag.*, vol. 56, no. 11, pp. 3485–3493, Nov. 2008.

[18] M. A. Qureshi, C. H. Schmidt, and T. F. Eibert, "Efficient near-field far-field transformation for nonredundant sampling representation on arbitrary surfaces in near-field antenna measurements," *IEEE Trans. Antennas Propag.*, vol. 61, no. 4, pp. 2025–2033, Apr. 2013.

[19] *IEEE Recommended Practice for Near-Field Antenna Measurements*, Standard 1720–2012, Dec. 2012, p. 102.

[20] M. Salucci, M. D. Migliore, G. Oliveri, and A. Massa, "Antenna measurements-by-design for antenna qualification," *IEEE Trans. Antennas Propag.*, vol. 66, no. 11, pp. 6300–6312, Nov. 2018.

[21] M. D. Migliore, M. Salucci, P. Rocca, and A. Massa, "Truncation-error reduction in antenna near-field measurements using an overcomplete basis representation," *IEEE Antennas Wireless Propag. Lett.*, vol. 18, no. 2, pp. 283–287, Feb. 2019.

[22] M. Salucci, M. D. Migliore, P. Rocca, A. Polo, and A. Massa, "Reliable antenna measurements in a near-field cylindrical setup with a sparsity promoting approach," *IEEE Trans. Antennas Propag.*, vol. 68, no. 5, pp. 4143–4148, May 2020.

[23] A. Massa, P. Rocca, and G. Oliveri, "Compressive sensing in electromagnetics—A review," *IEEE Antennas Propag. Mag.*, vol. 57, no. 1, pp. 224–238, Feb. 2015.

[24] S. Ji, Y. Xue, and L. Carin, "Bayesian compressive sensing," *IEEE Trans. Signal Process.*, vol. 56, no. 6, pp. 2346–2356, Jun. 2008.

[25] *Altair Feko*, Dept. Altair Feko., Altair Eng., Troy, MI, USA, 2020. [Online]. Available: www.altairhyperworks.com/feko